Mars Reconnaissance Orbiter Radio Science Gravity Investigation

Maria T. Zuber,[1] Frank G. Lemoine,[2] David E. Smith,[2] Alex S. Konopliv,[3] Suzanne E. Smrekar,[3] and Sami W. Asmar[3]

Received 23 September 2006; revised 22 December 2006; accepted 3 April 2007; published 30 May 2007.

[1] The objectives of the Mars Reconnaissance Orbiter (MRO) Radio Science Gravity Investigation are to improve knowledge of the static structure and characterize the temporal variability of the Martian gravitational field relevant to the planet's internal dynamics, the structure and dynamics of the atmosphere, and the orbital evolution of spacecraft at Mars. The investigation will utilize range rate and range measurements from X-band and, when available, Ka-band tracking systems of the MRO spacecraft. MRO will enable a considerable improvement in the spatial resolution and quality of Mars' global gravity field. The low orbital periapsis of MRO ($\sim$255 km) will yield gravity maps suitable for study of regional ($\sim 10^2$ km) structure of the crust and lithosphere. The addition of tracking data from the Mars Global Surveyor and Mars Odyssey spacecraft, also currently orbiting Mars, will be useful in decorrelating errors in spherical harmonic coefficients of the gravity field that will improve the quality of the static field. Studies of the low-degree gravity field combined with measurements of rotational dynamics will permit insight about the structure of Mars' deep interior. Changes in the low-degree spherical harmonic coefficients of the Martian gravity field and in polar mass anomalies will be used to track the seasonal cycle of CO_2 exchange with the surface. Measurements of spacecraft drag will be used to estimate density variations in the atmosphere relevant to weather patterns and aerobraking of future spacecraft. Tracking observations will also be used to improve the ephemeris of Mars and the masses of the Martian moons.

Citation: Zuber, M. T., F. G. Lemoine, D. E. Smith, A. S. Konopliv, S. E. Smrekar, and S. W. Asmar (2007), Mars Reconnaissance Orbiter Radio Science Gravity Investigation, *J. Geophys. Res.*, *112*, E05S07, doi:10.1029/2006JE002833.

1. Introduction: Overview

[2] Mars has exhibited a rich and varied evolution that has involved the interplay of its deep interior, lithosphere, cryosphere, hydrosphere, and atmosphere [*Kieffer et al.*, 1992; *VanDecar et al.*, 2001]. For the first time, space geodetic observations from orbiting spacecraft are achieving sufficiently high precision to enable measurements [*Smith et al.*, 1999a, 1999c, 2001b; *Lemoine et al.*, 2001; *Tyler et al.*, 2001; *Yuan et al.*, 2001; *Konopliv et al.*, 2006] relevant to the planet's internal structure, atmospheric dynamics, and cycles of volatiles [*Folkner et al.*, 1997b; *Zuber et al.*, 2000; *Zuber*, 2001; *Smith et al.*, 2001a; *Yoder et al.*, 2003]. Such measurements hold the promise of advancing understanding of Mars' interior, the interplay of the solid planet and its volatile reservoirs, and the planet's coupled thermal, rotational and climatic evolution. To take advantage of the emerging opportunity afforded by precise tracking of Mars orbiters, the Radio Science (RS) Gravity Investigation of the Mars Reconnaissance Orbiter (MRO) mission [*Zurek and Smrekar*, 2007] will utilize the spacecraft's Radio Frequency (RF) Telecommunications Subsystem to map Mars' static gravity field, to measure the temporal variability of the gravitational field, and to measure the atmospheric drag at spacecraft altitude.

[3] This investigation will combine Doppler range rate and range tracking data from MRO with similar observations from the Mars Global Surveyor (MGS) [*Albee et al.*, 2001] and Mars Odyssey (ODY) [*Saunders et al.*, 2004] missions. The combined analysis will maximize the geophysical science return of all three missions because solutions will be based on high-quality tracking from multiple spacecraft, which serves to mitigate systematic errors and decorrelate certain terms in the gravity field. In addition, the combination of data sets provides a longer time series from which to track temporal changes in the long-wavelength gravity field.

[4] The investigation will provide an improved static gravity field for Mars that will improve navigation of future Mars orbiters and surface targeting as well as enable more insightful models of Martian internal and thermal evolution

[1]Department of Earth, Atmospheric and Planetary Sciences, Massachusetts Institute of Technology, Cambridge, Massachusetts, USA.
[2]Solar System Exploration Division, NASA Goddard Space Flight Center, Greenbelt, Maryland, USA.
[3]Jet Propulsion Laboratory, Pasadena, California, USA.

Copyright 2007 by the American Geophysical Union.
0148-0227/07/2006JE002833

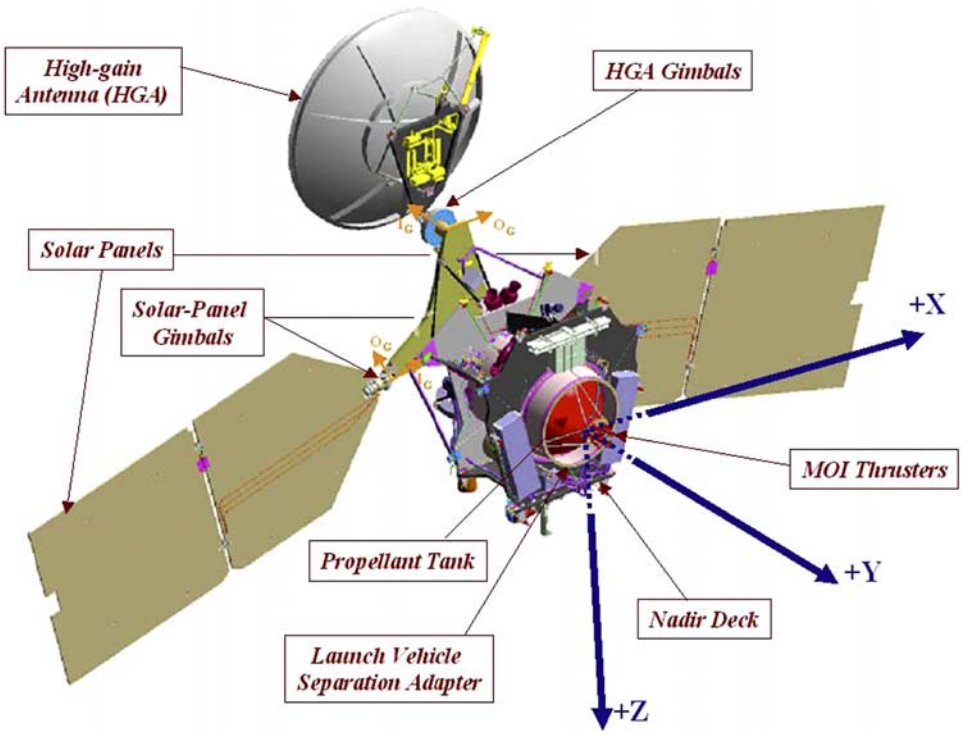

Figure 1. Schematic of the MRO spacecraft showing the position of the HGA [*You et al.*, 2005].

[*Phillips et al.*, 2001; *Zuber et al.*, 2000; *Zuber*, 2001]. Time variations in the gravity field will provide a quantitative measure of mass variations due to the seasonal cycle of CO_2 exchange between the atmosphere and cryosphere. Measurements of spacecraft drag from Doppler tracking will provide measurements of average atmospheric density at higher altitudes than possible with accelerometer measurements [*Tracadas et al.*, 2001; *Mazarico et al.*, 2007] and will have relevance to aerobraking, entry, descent and landing, and ultimate aerocapture of future Mars spacecraft.

2. Tracking of the Mars Reconnaissance Orbiter

2.1. Spacecraft Telecom Subsystem

[5] The MRO Primary Telecom Subsystem operates at X-Band, with an uplink frequency of 7.2 GHz and a downlink frequency of 8.4 GHz. The tracking system utilizes MRO's 3-m-diameter high-gain antenna (HGA) (Figure 1) and a 100-Watt X-band radio traveling wave tube amplifier (TWTA) to transmit signals to Earth. In addition, MRO also has two broader-beam, low-gain antennas that are mounted on the HGA dish for lower-rate communication and for use in critical maneuvers (i.e., orbit insertion) or during spacecraft upsets. Communication with Earth is accomplished using 34-m and 70-m antennas of NASA's Deep Space Network (DSN) stations in Goldstone, California, Madrid, Spain, and Canberra, Australia.

[6] MRO also includes a technology demonstration experiment consisting of a Ka-band transponder on the spacecraft that produces an RF downlink at a frequency of 32.2 GHz [*Shambayati et al.*, 2006]. The Ka-band subsystem has a 35-Watt TWTA to amplify its signal so that it can be downlinked to DSN antennas that have been modified to receive at that frequency.

2.2. Data Types

[7] The tracking data is used by the MRO Navigation Team to determine the velocity of the spacecraft and its position in inertial space. Range rate is measured from the downlink signal transmitted from the spacecraft's X-band transponder. The frequency of the signal is Doppler shifted, and the magnitude of the Doppler shift yields the velocity of the spacecraft in the line of sight to the observer. The velocity of the spacecraft in orbit around Mars changes due to forces acting on the spacecraft that include gravitational perturbations due to Mars' mass distribution, spacecraft maneuvers, and radiation pressure.

[8] Another data type is the range from the ground tracking station to the spacecraft. Ranging measurements are made via standard sequential tone ranging. The DSN transmits a series of ranging tones; the on-board transponder receives these tones and re-transmits them back to Earth. The difference between the time of transmission of the ranging tones and the time of reception, along with knowledge of the transmission delay within the spacecraft, yields the spacecraft range.

2.3. Doppler Error Sources

[9] The accuracy of the Doppler measurement is limited by the performance of the X-band system and is specified to be ± 0.1 mm s^{-1} over a 60-s integration period [*You et al.*, 2005]. Sources of measurement error include: thermal noise, solar plasma, ionosphere, troposphere, spacecraft delay variation, and ground station delay uncertainty [*Sniffin et al.*, 2000; *Asmar et al.*, 2005]. These errors are discussed

Table 1. Doppler Measurement Error Parameters

Parameter	Value
$f_{U/L}$	7.2 GHz
$f_{D/L}$	8.4 GHz
G	1.17
P_c/N_o	28/34 dB (uplink/downlink)
C_{freq}	5.5×10^{-5}
TEC	1×10^{16} to 4×10^{18} electrons m^{-2}

briefly below and have been addressed specifically for the MRO mission by *Lee* [2002].

[10] Thermal noise induces phase jitter in the carrier tracking loops in the DSN receiver and spacecraft telecom system. The error is [*Sniffin et al.*, 2000]

$$\sigma_\nu = \frac{c}{2\sqrt{2}\pi f_c T}\sqrt{\frac{1}{\rho_L} + \frac{G^2 B_L}{(P_c/N_o)_{U/L}}}, \tag{1}$$

where T is the integration time, G is the transponder ratio, f_c is the downlink carrier frequency, B_L is the spacecraft transponder carrier loop bandwidth, $(P_c/N_o)_{U/L}$ is the uplink signal/noise ratio and

$$\rho_L = \frac{1}{B_L}\left(\frac{P_c}{N_o}\right)_{D/L} \tag{2}$$

is the downlink (D/L) carrier signal/noise ratio that assumes a residual carrier tracking loop is used at the ground receiver. The propagation loss will vary as a function of the distance between the orbiter and Earth, which is approximated by the Earth to Mars range while the orbiter is circling Mars.

[11] Solar plasma causes scintillation in the carrier that depends on the Sun-Earth-Probe angle, θ_{SEP}. The associated error in the range $5° \leq SEP \leq 27°$ is [*Sniffin et al.*, 2000]

$$\sigma_\nu = \frac{0.73c\left(C_{freq}\right)^{1/2}\left[\sin(\theta_{SEP})\right]^{-1.225}}{f_c T^{0.175}}, \tag{3}$$

where C_{freq} is a constant that depends on the uplink/downlink bands.

[12] The passage of the tracking signal through the ionosphere also results in scintillation that produces phase fluctuations. The error can be expressed [*Sniffin et al.*, 2000]

$$\sigma_\nu = \frac{\sigma_{\Delta t} c}{2T}, \tag{4}$$

where Δt is the group delay (in seconds) caused by the ionosphere at frequency, f, c is the speed of light and

$$\Delta t = \frac{1.345 \times 10^{-7}}{f^2} TEC, \tag{5}$$

where TEC is the total electron content along the propagation path. In equation (4) $\sigma_{\Delta t}$ is bounded by the maximum and minimum values of Δt.

[13] The troposphere also contributes phase fluctuations to the uplink and downlink. At low frequencies (S-band; 2.6 GHz) solar plasma and ionospheric effects dominate the Doppler error and at high frequencies (Ka-band; 32.2 GHz) tropospheric effects dominate [*Sniffin et al.*, 2000]. The tropospheric delay depends on the water vapor content of the atmosphere in the propagation path, mainly below altitudes of 8–15 km. Atmospheric delays are a function of elevation angle of the spacecraft above the horizon as viewed by the ground station, with larger effects at lower angles due to the longer path length through the atmosphere as well as increased ground noise received by antenna sidelobes.

[14] The spacecraft experiences delay variation from changes in the group delay of components primarily due to temperature. Temperature changes in the waveguides, the transponder, and power amplifiers all affect the Doppler measurement. These delays are measured during spacecraft testing.

[15] Finally, the ground system (DSN) contributes to Doppler noise due to temperature and location uncertainties [*Miller*, 1993]. The frequency stability of the ground station is sensitive to stability of various components including the exciter, test translator, X-band maser, VLBI/RS downconverter, IF/video downconverter, narrow-band occultation converter, spectrum-processor assembly and system cables. A detailed assessment from the Mars Global Surveyor mission showed the total Doppler error contribution from the DSN not to exceed 0.05 mm s^{-1} [*Short et al.*, 1996].

[16] Relevant parameters for X-band tracking are discussed extensively by *Lee* [2002] and major parameters are listed in Table 1. Estimates of the contribution of each of these error sources, for a range of elevation (ELV) angles, SEP = 90° and an integration interval of 60 s, are given in Table 2. The error analysis indicates that solar plasma is the dominant error source for MRO. Use of Ka-band tracking (Ka-band downlink coherent along with a Ka-band uplink) would reduce the solar plasma effect by about a factor of four and the effect of the ionosphere by about a factor of 16. For the Ka downlink only the noise reduction will be less. The greatest improvement in S/N for the Ka-band is expected to be at smaller sun angles where the effect of solar plasma is considerable. It is possible to combine X- and Ka-band downlinks to calibrate the solar plasma and ionosphere, but the lack of a Ka-band uplink on MRO dictates that a complete cancelation of these effects is not possible. However, on the basis of the demonstrated performance of telecon systems in previous and ongoing missions [*Tyler et al.*, 2001; *Srinivasan et al.*, 2007], the dual frequency analysis is not required to achieve the Doppler accuracy required by the MRO mission. Figure 2 shows examples of two- and three-way Doppler residuals during MRO's cruise to Mars. The data have RSS scatter of 0.02 mm s^{-1} that meets the required quality of the tracking measurements.

2.4. Observation Strategy

[17] There is no direct commanding of the telecom system but the RS Gravity Investigation will benefit from optimal observation strategies to maximize the science recovery. The Doppler tracking requirement is a minimum of one full (~12 hour) DSN pass per day. The minimum

Table 2. Estimated Contributions to Doppler Measurement Error

Error Source	ELV = 30°, mm s^{-1}	ELV = 60°, mm s^{-1}	ELV = 90°,[a] mm s^{-1}
Thermal noise	5.48×10^{-3}	5.43×10^{-3}	5.45×10^{-3}
Solar plasma	4.54×10^{-2}	4.54×10^{-2}	4.54×10^{-2}
Ionosphere	1.97×10^{-2}	1.28×10^{-2}	1.12×10^{-2}
Troposphere	5.99×10^{-2}	3.46×10^{-2}	3.00×10^{-2}
S/C variation	4.95×10^{-2}	7.04×10^{-2}	7.26×10^{-2}
DSN	4.09×10^{-2}	4.09×10^{-2}	4.09×10^{-2}
RSS	0.01	0.01	0.01

[a]Assumes 10-s integration time. Delay values are typically expressed in terms of spacecraft velocity. Note that there is a factor of two difference when converting the frequency of delay, which contains contributions from two-way propagation, to velocity. From *Lee* [2002].

amount of ranging required is the equivalent of 1 hour of quality ranging data every 5 days, spread out over visible parts of several orbits; distributed data collection mitigates bias errors associated with a single tracking station on a single pass. There is also a desire to distribute observations among all DSN stations, again to minimize station biases.

[18] In practice, during typical mapping operations, MRO will have two 8-hour-long X-band passes per day using the DSN's 34-m antennas, and three X-band passes per week using the DSN's 70-m antennas. In addition, two Ka-band passes per week are currently planned.

[19] The RS Gravity Investigation relies on MRO's baseline X-band system, but the Team plans to utilize to the extent possible Ka-band tracking from the technology demonstration experiment. Ka-band tacking, because of its high frequency, is less susceptible to noise from solar plasma and in addition allows transmission at much higher data rates than X-band. The science objectives of the Gravity Investigation do not depend on the acquisition of Ka-band tracking data, but science return is expected to be enhanced by its use. As part of its investigation the RS Gravity Team will assess the utility of Ka-band observations for gravity field modeling and spacecraft precision orbit determination.

[20] The Ka-band system experienced an anomaly during the mission aerobraking phase in June 2006. Detailed troubleshooting will occur once the mapping mission begins and if function is not regained the system could switch to the backup.

[21] While the MRO RS Gravity Investigation will benefit from high-quality tracking and significant tracking time, modeling MRO tracking data may well be more challenging than for other Mars missions due to frequent off-nadir spacecraft rolls, frequent solar array and HGA motion, and greater drag due to the low periapsis altitude.

3. Methodology

3.1. Precision Orbit Determination

[22] Scientific analysis of radio tracking data requires first the determination of precision orbits for the MRO spacecraft. The precision orbit determination process requires the full integration of the spacecraft trajectory from an initial state, with application of various physical models to account for the non-conservative forces that act on the spacecraft. The GEODYN/SOLVE programs [*Pavlis et al.*, 2001, 2006] at NASA/GSFC and DPODP program [*Moyer*, 1971] at the Jet Propulsion Laboratory are used in the determination of precision orbits. Both software systems employ a Bayesian least-squares approach to determine the convergence of spacecraft orbit segments referred to as arcs. In practice arcs are usually about 5-days in length.

[23] The physical models that are utilized in the precision orbit determination process include an a priori gravitational model for Mars; third-body perturbations from the sun, moon, all planets in the solar system, and the Martian moons, with positions from the JPL DE410 ephemeris [*Standish*, 2004]; relativistic correction to the force model (due to the modification of the Mars central body term) and in the measurement model (for light time and range corrections, combined with the ephemerides); the effect of the Mars solid tide, k_2; corrections for solar and Mars-reflected albedo and infrared radiation; DSN ground station position corrections due to solid tides, ocean loading, and tectonic

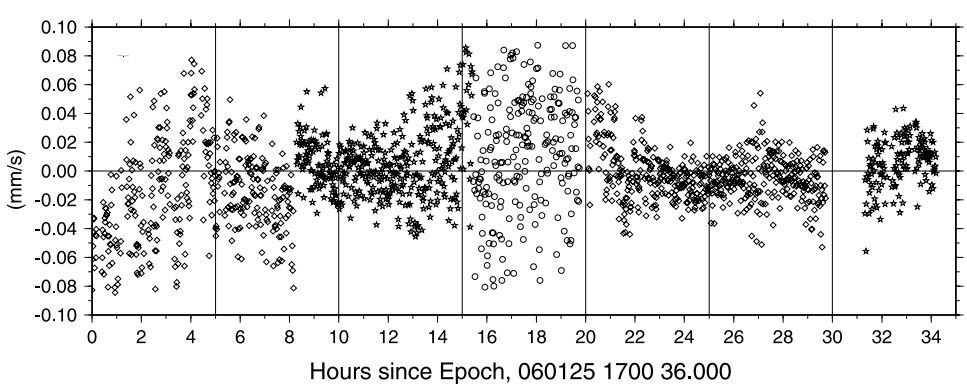

Figure 2. Example of Doppler residuals for MRO during cruise to Mars. The sampling interval is 60 s.

plate motions; corrections to the radio signal for its propagation through the troposphere, dependent on local weather; and a correction for atmospheric drag. In addition, angular momentum desaturations of the spacecraft's momentum wheels that cause small perturbations on the spacecraft orbit are also estimated.

[24] As discussed later, several of the above parameters, such as k_2 and the drag coefficient provide information of scientific interest and are adjusted and improved as part of the gravity field estimation procedure.

3.2. Gravitational Potential

[25] The expression for the gravitational potential, U, is a solution to Laplace's equation, which for a spherical planet takes the form of a series of spherical harmonics [*Heiskanen and Moritz*, 1967; *Kaula*, 1966]

$$U(r,\theta,\lambda) = \frac{GM}{r}\left\{1 + \sum_{l=2}^{\infty}\left(\frac{R}{r}\right)^{l}\sum_{m=0}^{l} \cdot \left[\left(\bar{C}_{l,m}\cos m\lambda + \bar{S}_{l,m}\sin m\lambda\right)\bar{P}_{l,m}(cos\theta)\right]\right\}, \quad (6)$$

where G is the universal constant of gravitation, M is the total planetary mass; R is the reference equatorial radius, $\bar{P}_{l,m}$ are normalized associated Legendre functions of degree l and order m; r, λ, and θ are the body-fixed coordinates of radial distance, longitude, and co-latitude; and $\bar{C}_{l,m}$ and $\bar{S}_{l,m}$ are the normalized Stokes coefficients that contain the information about the spatial distribution of planetary mass anomalies, with larger values of l and m corresponding to progressively smaller spatial scales. In the following discussion we assume all coefficients are normalized [*Kaula*, 1966] and omit the over bars.

[26] The special case of $m = 0$ corresponds to the zonal coefficients $C_{l,0}$, which provide information about latitudinal variations in the mass distribution. Setting $m = 0$ removes the dependence on longitude. Because the Mars CO_2 cycle is manifest primarily by the movement of volatile mass between the north and south polar regions, it is these zonal coefficients that are of greatest interest in seasonal mass exchange analyses.

[27] In practice, the spherical harmonic solution comes from inversion of the normal equations that compose the (sparse) observation matrix. This matrix contains the tracking observations that are weighted according to quality and distribution [*Balmino et al.*, 1982; *Smith et al.*, 1993]. The solution also provides estimates of dynamical parameters including the pole position, rotation rate, solid body tide k_2, and masses of Phobos and Deimos [*Lemoine et al.*, 2001; *Yuan et al.*, 2001; *Konopliv et al.*, 2006].

[28] Evaluation of the quality of the gravity fields is accomplished by (1) computation of orbit overlaps, e.g., the difference in radial, along-track and across-track position between predicted and observed orbits, and (2) error analysis using the covariance matrix.

3.3. Data Processing

[29] The RS Gravity Team will process the Doppler and range observations as they are obtained and first produce precision orbits for the MRO spacecraft. Subsequent analysis will include the development of updated gravity models and dynamical parameter estimation, including error estimation. The Team will produce a new gravity model as soon as feasible during the Primary Science Phase of the MRO mission (e.g., using the first month of mapping data), and another at the end of mission. Additional models will be produced and disseminated on a best efforts basis.

4. Science Investigation

4.1. Static Gravity Field

[30] The Mariner 9 and Viking 1 and 2 orbiters yielded global gravity fields of Mars based on S-Band Doppler tracking data (2.1 and 2.3 GHz for uplink and downlink, respectively) with an accuracy of $\sim$1 mm s^{-1} averaged over 10 s. The fields were of moderate spatial resolution: degree and order 18–50, corresponding to spatial resolution of 600–210 km [*Balmino et al.*, 1982; *Smith et al.*, 1993]. However, due to variable spatial coverage produced by inclined, elliptical spacecraft orbits, solutions above about degree 20 required the imposition of an a priori (aka "Kaula") constraint [*Kaula*, 1966] on the covariance matrix to assure convergence.

[31] The MGS mission [*Albee et al.*, 2001] enabled a significant improvement in the global gravity field of Mars [*Smith et al.*, 1999a; *Lemoine et al.*, 2001; *Yuan et al.*, 2001] for two primary reasons: (1) the radio system utilized X-band tracking that was less susceptible to solar plasma noise than previous S-band systems, which resulted in accuracy improved to better than 0.1 mm s^{-1}, and (2) the uniform coverage provided by MGS's near-polar, circular ($\sim$400-km-altitude) orbit [*Tyler et al.*, 1992, 2001]. These high-quality Doppler observations were used to construct models of the Martian gravity field by groups at NASA/GSFC [*Lemoine et al.*, 2001] and JPL [*Yuan et al.*, 2001]. Both fields lack a priori constraints below about degree 60 (spatial resolution $\sim$180 km). Because the constraint suppresses power in certain coefficients, geophysical interpretation at high degrees and orders (i.e., the shortest resolvable length scales) must be done with caution. The MGS gravity fields are interpretable in a geophysical sense to resolution of $\sim$160 km [*Zuber et al.*, 2000; *Zuber*, 2001].

[32] Mars Global Surveyor also demonstrated for the first time on a planetary mission how spacecraft position measurements determined by laser altimetry [*Smith et al.*, 2001b] at orbital "crossover" points [*Rowlands et al.*, 1999; *Neumann et al.*, 2001] could be used to improve the Martian gravity field [*Lemoine et al.*, 2001].

[33] Most recently, X-band tracking data from the ODY spacecraft was added to MGS tracking to improve the Martian gravity field and estimates of dynamical parameters [*Konopliv et al.*, 2006], as well as the ephemeris [*Standish*, 2004] and tidal parameters [*Yoder et al.*, 2003]. The addition of another satellite with high-quality X-band tracking enables certain errors to be decorrelated and so certain spherical harmonic terms to be better resolved. But since ODY is in a very similar orbit to MGS the spatial resolution is not markedly improved. Current models are based on the IAU 2000 Mars pole and prime meridian and the reference radius of Mars from the Mars Orbiter Laser Altimeter [*Smith et al.*, 2001b]. Free-air gravity anomalies based on current knowledge of the gravity field are shown in Figure 5.

[34] Figure 3 shows power and error spectra of the Mars gravity field for the case of no a priori constraint [*Lemoine*

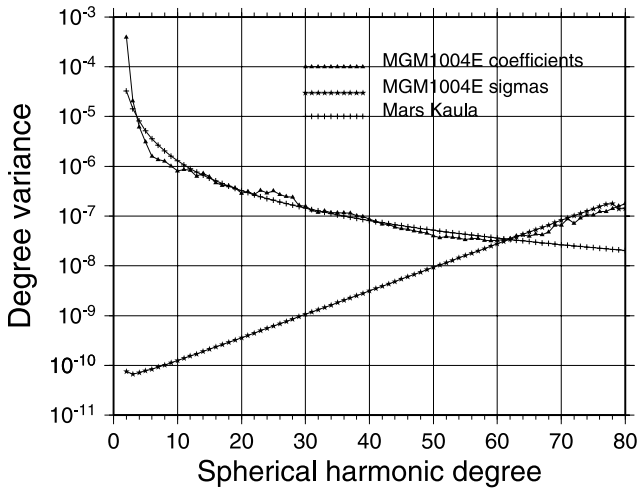

Figure 3. RMS spherical harmonic power and standard deviation as a function of spherical harmonic degree for Mars gravity model GMM-2B without a Kaula constraint. From *Lemoine et al.* [2001].

et al., 2001]. The degree variance of the power spectrum, σ_l^2, is defined as

$$\sigma_l^2 = \left[\sum_{m=0}^{l}\left(C_{l,m}^2 + S_{l,m}^2\right)\right]/(2l+1). \quad (7)$$

[35] Note that the observed power of the gravity field matches the empirical expected decay spectrum ($13 \times 10^{-5}/n^2$) of the power law (Kaula's Rule) [*Kaula*, 1966] up to about degree and order 60. At this point the noise in the unconstrained solution, typified by the error spectrum, equals the magnitude of the signal. The MRO mission, with its higher signal strength due to the large HGA, lower noise due to the addition of Ka-band tracking, and higher spatial resolution due to the lower spacecraft periapsis altitude compared to MGS and ODY, will result in a static gravity field with improved quality and spatial resolution. Figure 4 compares expected root mean square (RMS) accelerations and maximum resolution for geophysical interpretation. The spatial resolution of MRO fields should be approximately 100 km.

4.2. Internal Structure

4.2.1. Crust and Lithosphere

[36] The combination of gravity [*Smith et al.*, 1999a; *Lemoine et al.*, 2001; *Yuan et al.*, 2001] and topography [*Smith et al.*, 1999c, 2001b] from MGS resulted in the first reliable models of the crustal and lithospheric structure of Mars [*Zuber et al.*, 2000; *Zuber*, 2001; *McGovern et al.*, 2002; *McKenzie et al.*, 2002; *Turcotte et al.*, 2002]. Various models of crustal structure show the crust to consist of two spatially-distinctive provinces that correspond broadly to the planet's hemispheric dichotomy in surface geology and crater density. In addition, transfer function analyses of gravity and topography demonstrated that the effective elastic thickness, which represents the "thermal age" of the lithosphere [*Turcotte and Schubert*, 1981], reflects the time of surface or subsurface loading rather than of crustal formation [*Zuber et al.*, 2000].

[37] Regional inversions of gravity and topography in areas of large surface or subsurface relief, such as impact basins, have been shown to require corrections for finite amplitude effects when there are large surface or subsurface topography [*Wieczorek and Phillips*, 1998; *Lowry and Zhong*, 2003] in order to obtain plausible estimates of crustal density and lithosphere thickness [*McKenzie et al.*, 2002; *McGovern et al.*, 2002; *Wieczorek and Zuber*, 2004]. Regional studies have examined variations in the isostatic gravity field (with effects of topography and crustal compensation removed) that show numerous small-scale density anomalies, some of which can be related to regional geology [*Dombard et al.*, 2004; *Kiefer*, 2004; *Smrekar et al.*, 2004; *Searls et al.*, 2006]. Variations in elastic thickness also illuminate the local geologic history [*Belleguic et al.*, 2005; *Hoogenboom and Smrekar*, 2006; C. A. E. Milbury et al., Lithospheric structure in the eastern region of Mars' dichotomy boundary, submitted to *Journal of Geophysical Research*, 2006]. Tracking from MRO (Figure 4) will enable the resolution of spatial block sizes as short as 100 km, which will permit analyses of even more localized individual tectonic and volcanic structures.

4.2.2. Deep Interior

[38] Information on the nature of the deeper interior comes from a combination of the moment of inertia factor, $C/M\,R^2$ where C is the polar moment of inertia, and M and R are the mass and radius of Mars, and the tidal Love number, k_2, which is sensitive to the thickness and rigidity of the mantle and the radius and state of the core [*Kaula*, 1979; *Bills*, 1990; *Folkner et al.*, 1997a].

[39] Determination of the moment of inertia factor requires knowledge of the planetary flattening $J_2 = -C_{2,0}$, which comes from the precession of the node of satellite orbits, and the dynamical ellipticity that comes from the precession of the spin pole [*Folkner et al.*, 1997a]. Tracking of the Viking and Pathfinder landers was used to estimate the precession of Mars, which led to the first reliable

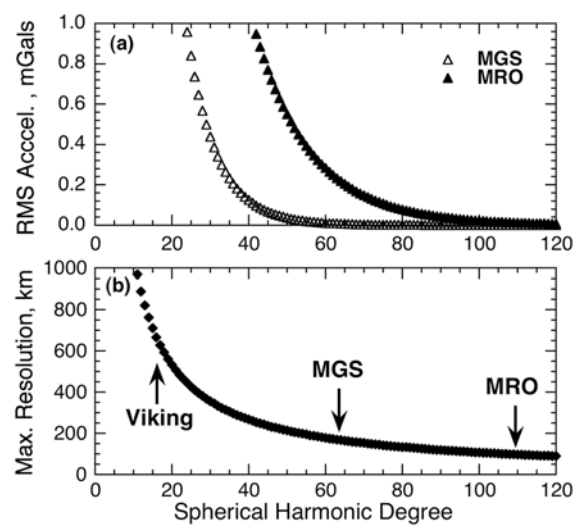

Figure 4. Expected (a) RMS accelerations and (b) maximum interpretable spatial resolution of MRO gravity in comparison to selected previous missions.

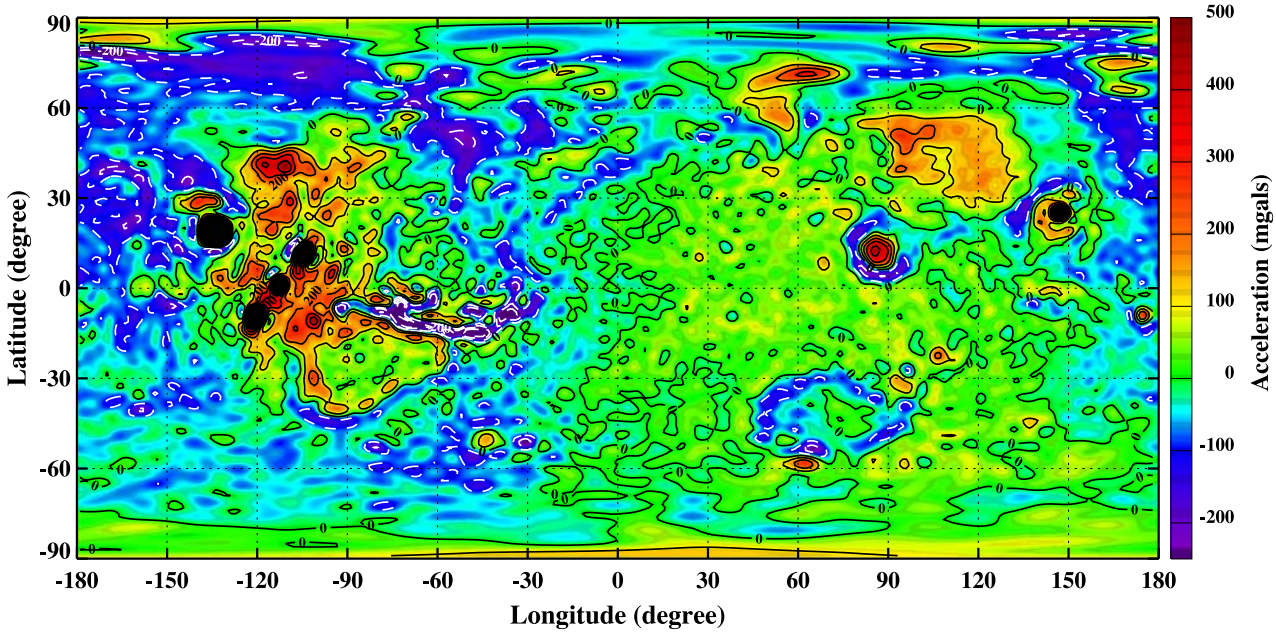

Figure 5. Free-air surface anomalies of the MGS95J gravity model to degree and order 70 [*Konopliv et al.*, 2006].

estimate of the moment inertia factor $C/MR^2 = 0.3654 \pm 0.0008$ [*Folkner et al.*, 1997b].

[40] The response of the solid planet to solar tides was detected by the MGS spacecraft [*Yoder et al.*, 2003], and a refined solution obtained from combining MGS and ODY yielded an improved estimation of the tidal Love number $k_2 = 0.148 \pm 0.009$ [*Konopliv et al.*, 2006]. This value includes correction for the influence of atmospheric tides, frictional dissipation and anelastic softening, and together with the moment of inertia factor currently provides the best constraint on the size of Mars' fluid core. Figure 6 uses k_2 and C/MR^2 in the context of interior models based on geochemical constraints [*Sohl and Spohn*, 1997] to indicate that even with firm estimates of the required parameters the uncertainty in core radius is considerable, with an allowable range of 1600 to 1810 km. MRO can be expected to make a modest refinement in this range but significant improvement will require surface seismic and/or geodetic experiments [cf. *Lognonne and Mosser*, 1993; *Lognonne et al.*, 1999; *Van Hoolst et al.*, 2000; *Barriot et al.*, 2001; *Dehant et al.*, 2004].

4.3. Time-Variable Gravity and the Seasonal CO_2 Cycle

[41] Approximately 25% of the CO_2 in the Martian atmosphere moves from one pole to the other over the course of a Martian year [*James et al.*, 1992]. This seasonal signal was first observed in a local sense as a variation of surface pressure at the Viking landing sites [*Hess et al.*, 1979, 1980; *Leovy*, 1985; *Zurek et al.*, 1992]. A seasonal pressure change was also observed at the Pathfinder landing site for a fraction of a Martian year [*Schofield et al.*, 1997]. Carbon dioxide, and to a lesser extent water, sublimates from the summer polar region and moves toward the equator, decreasing the mass at the pole while increasing the mass at the equator thereby increasing the "flattening" of the gravity field. Also, as the atmospheric material moves toward the winter pole some of it condenses out as ice (CO_2 and to a much lesser extent H_2O), forming an additional mass layer on the surface, thereby increasing the mass at the winter pole at the expense of mass at the equator and the summer pole. This further changes the "flattening" or degree-2 zonal term of equation (6), as well as other low-degree (long-wavelength) terms [*Folkner et al.*, 1997b; *Smith et al.*, 1999a, 1999b, 2001a; *Yoder et al.*, 2003; *Karatekin et al.*, 2005; *Konopliv et al.*, 2006]. In comparison to other terms in the Martian gravity field, these long-wavelength signals have the largest amplitudes because they are the most sensitive to global changes in the density distribution. Fortuitously, these long-wavelength zonal signals are also the best determined in spherical harmonic models because the long wavelengths are sampled whenever the spacecraft is being tracked [*Smith et al.*, 1999b].

[42] Changes in the $C_{2,0}$ and $C_{3,0}$ are now routinely being recovered from MGS and ODY [*Konopliv et al.*, 2006; *Zuber and Smith*, 2006], as are "mascon" anomalies that correspond to the spatial extent of Mars' seasonal frost caps [*Zuber and Smith*, 2006]. The determination of temporal coefficients is accomplished in two ways: by solving for the coefficients directly holding other parameters fixed, and by solving for amplitude and phase assuming a harmonic variation of the expected functional form. Figure 7 demonstrates that the change in the $C_{3,0}$ coefficient is in good agreement with the change expected by general circulation model (GCM) simulations of the CO_2 cycle. The pattern for the temporal change in the $C_{2,0}$ coefficient is more complex than predicted by the GCM [*Smith et al.*, 2001a; *Yoder et al.*, 2003; *Konopliv et al.*, 2006; *Zuber and Smith*, 2006], indicating that other processes also influence the temporal variation of this coefficient. The independent measurement by MRO, in its considerably different orbit from MGS and ODY, will be helpful in understanding the contributions to

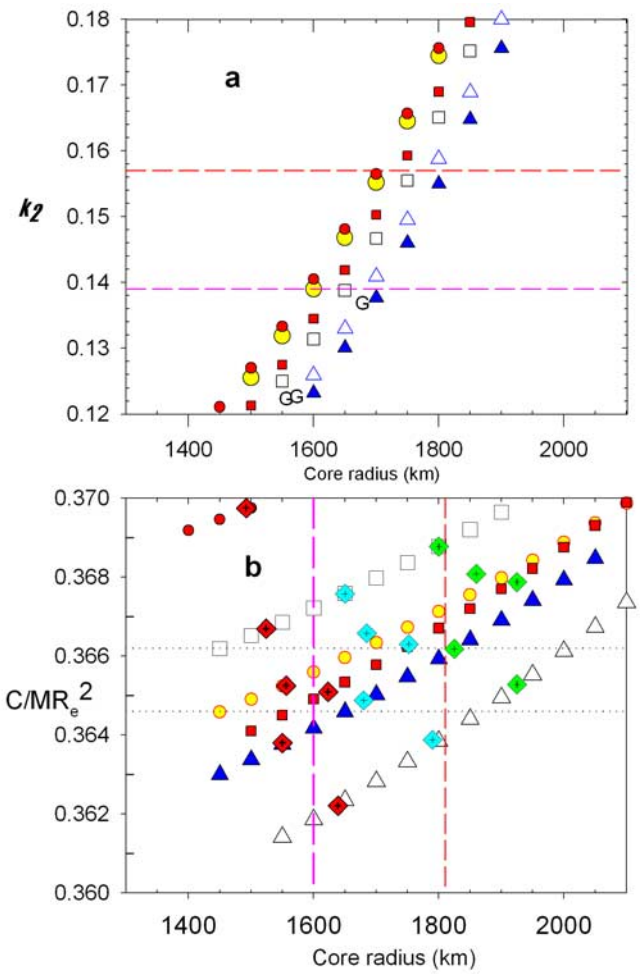

Figure 6. Model estimates of (a) the elastic Love number, k_2, and (b) moment of inertia, $C/M\,R^2$, versus core radius for a representative suite of structural models of Mars. These models vary the mantle composition parameter χ_M = Mg/(Mg + Fe); χ_M = 85% (triangle), 80% (box), and 75% (circle), temperature ΔT = 200 K (red, yellow), 0 (white), and −200 K (blue). The assumed crustal thickness is 50 km except for χ_M = 75%, and ΔT = 200 K and h_{cr} = 100 km (yellow circle). In Figure 6b, diamonds correspond to core χ_c = Fe/(Fe + FeS) = 25% (red), 50% (cyan), and 75% (green). From *Konopliv et al.* [2006].

that term, and hence improving the seasonally-varying mass estimation.

4.4. Spacecraft Drag and Atmospheric Density

[43] At high altitudes, the Martian atmosphere is not well sampled spatially or temporally. The Viking 1 and 2 and Mars Pathfinder landers each provided one vertical profile from accelerometer (and, in the case of Viking, mass spectrometer) measurements during entry and descent under solar minimum conditions [*Nier and McElroy*, 1977; *Seiff and Kirk*, 1977; *Magalhaes et al.*, 1999]. The MGS accelerometer provided almost global sampling of the Martian thermosphere below ~170-km altitude [*Tolson et al.*, 1999] during solar minimum to medium conditions. Doppler tracking can be used to measure the orbital decay due to drag, and hence air density.

[44] The orbital energy lost ($\Delta E = E_{i+1} - E_i$) can be calculated from the semi-major axis values at the preceding and following apoapsides as

$$\Delta E_i = \Delta E_{i+1} - E_i = -\frac{GM}{2}\left(\frac{1}{a_{i+1}} - \frac{1}{a_i}\right) < 0. \qquad (8)$$

[45] Together with a simple atmospheric exponential density model

$$\rho(z) = \rho_o \exp\left(-\frac{z - z_o}{H_o}\right), \qquad (9)$$

where ρ_o is the reference density, z and z_o are altitude and a reference altitude, and H_o is the reference scale height. Equation (8) can be used to obtain the energy lost by friction along the spacecraft trajectory arc, where each discretized 1-second segment contributes

$$dE_{dis} = \frac{1}{2} C_D A \rho(z) V(z)^2 ds \qquad (10)$$

to the total dissipated energy, E_{dis}. Here C_D is the drag coefficient, ds is the length of the segment, A is the cross-sectional area of the spacecraft, and V is spacecraft velocity. The atmospheric density, ρ_o, at the reference height, z_o, is adjusted so that $\Delta E = E_{dis}$. The density at periapsis can thus be obtained.

[46] An alternative is to use a theoretical expression by *King-Hele* [1987] that provides a direct relationship between the eccentricity, the change in semi-major axis, and the density at the periapsis assuming a linear relationship between scale height and altitude. Figure 8 compares densities of the Martian atmosphere from the Mars ODY spacecraft during its aerobraking phase. Both drag methods are in general agreement with results from direct measurements from the ODY accelerometer [*Keating et al.*, 2004], in terms of magnitude and trend. While atmospheric dynamics can result in complex changes in density, broader patterns such as solar cycle-related temperature and density variations have been identified in both accelerometer [*Withers*, 2006] and drag [*Forbes et al.*, 2006; *Lemoine et al.*, 2006; *Mazarico et al.*, 2007] measurements. While spacecraft accelerometers lose sensitivity above aerobraking periapsis altitudes (~170 km), the drag methods have been demonstrated to recover spacecraft density to mapping orbit altitudes (~400 km) [*Konopliv et al.*, 2006; *Mazarico et al.*, 2007] and are well suited to resolve atmospheric density at the orbital periapsis altitude of MRO. The use of Doppler observations to recover atmospheric density will work best when the atmospheric structure follows the assumed exponential structure, and is thus not well suited for particularly turbulent regions.

4.5. Other Objectives

4.5.1. Dynamics

[47] As atmospheric material moves over the surface of the planet, the angular momentum of the atmosphere changes and the rotation rate of the solid part of the planet

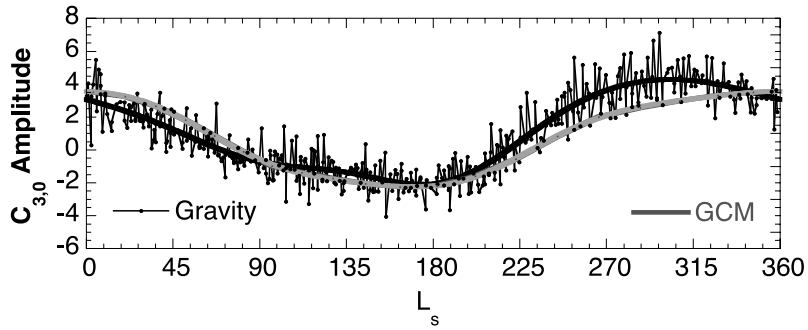

Figure 7. Temporal variation in the $C_{3,0}$ coefficient compared to that expected from a GCM simulation of the seasonal CO_2 cycle. After *Zuber and Smith* [2006].

compensates to conserve the planet's total angular momentum. Any imbalance in the distribution of atmospheric material with respect to the rotation pole introduces a torque on the rotation axis that excites polar motion. The global-scale gravitational and rotational effect is proportional to the ratio of the net amount of re-distributed mass to the total mass of the planet [*Chao and Rubincam*, 1990]. For the CO_2 exchange between the Martian atmosphere and cryosphere, this ratio is $\sim 1.3 \times 10^{-8}$, which is larger, by 1–2 orders of magnitude, than the largest effects on Earth associated with post-glacial rebound [*Rubincam*, 1984], the largest El Nino events [*Gross and Chao*, 1985] or major earthquakes [*Chao and Gross*, 1987]. As mass is seasonally redistributed on Mars, gravitational terms in addition to the flattening also change. The degree-1 terms indicate the movement of the center of mass in the established coordinate system, and the non-zonal degree-2 terms represent the orientation of principal axis with the coordinate system. The latter terms ($C_{2,1}$ and $S_{2,1}$) indicate how the gravity field is aligned with respect to the polar axis of the coordinate system and can therefore be related to polar motion. The displacement between the axes is given in radians by

$$\delta = \frac{\left(C_{2,1}^2 + S_{2,1}^2\right)^{1/2}}{C_{2,0}}, \tag{11}$$

and the phase or longitude by

$$\lambda = \tan^{-1}\left(\frac{S_{2,1}}{C_{2,1}}\right). \tag{12}$$

Polar motion has not yet been detected at Mars, from either landers or orbiters, but a 1–2 m signal is predicted from asymmetric changes in the polar caps [*Defraigne et al.*, 2000]. *Konopliv et al.* [2006] showed that Mars' free wobble is no greater than $\sim$20 cm. The refined rotation model from MRO will provide an improved reference to attempt to detect such expected small changes.

[48] The change in length of day (ΔLOD) caused by the variation in atmospheric pressure is proportional to the change in the gravitational flattening term ($\Delta J_2 = -\Delta\ C_{2,0}$,

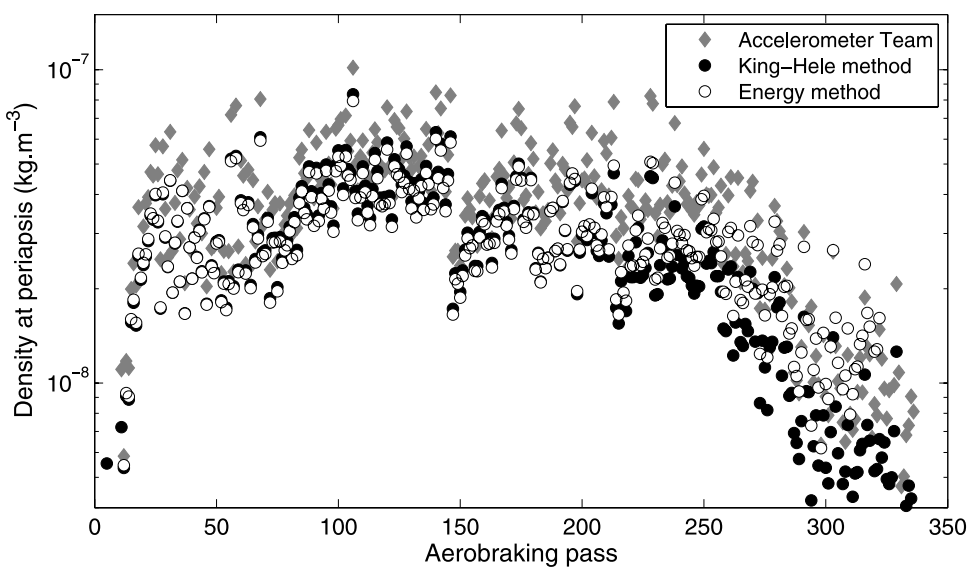

Figure 8. Atmospheric density at periapsis of the Mars Odyssey spacecraft using two atmospheric drag methods described in the text and the ODY accelerometer. The drag methods assume a scale height of 10 km. From *Mazarico et al.* [2006].

where $C_{2,0}$ is normalized.) Because the mass re-distribution associated with this pressure change occurs very close to the surface of Mars (in comparison to the planetary radius), ΔLOD can be expressed [*Chao and Gross*, 1987]

$$\Delta LOD(t) = LOD\left[\frac{2Ma^2\Delta J_2(t)}{3C}\right], \tag{13}$$

where C is the maximum moment of inertia. This expression represents the simplest case in which the length of day reflects only the change in J_2 associated with the cycle of CO_2 exchange. However, in practice there is an additional contribution to the LOD change associated with the wind angular momentum. Seasonal zonal winds, which are the primary cause of ΔLOD on Earth, were long thought to be much less important on Mars [*Folkner et al.*, 1997b]. There are no direct measurements of these winds, and the only estimates come from Martian GCMs. The calculated zonal wind values suggest annual amplitudes as large as one third of the total ΔLOD [*Van den Acker et al.*, 2002; *Sanchez et al.*, 2003]. Until zonal winds are measured directly the interpretation of internal structure from ΔLOD will be uncertain. Comparing the ΔLOD to the independently determined J_2 from MRO will permit these contributions to be estimated.

4.5.2. Ephemeris

[49] Precise knowledge of the heliocentric orbit (aka ephemeris) of Mars is important in its own right and because it influences the estimation of other important phenomena such as the masses of major main belt asteroids [*Hilton*, 1999] and the temporal gravity signal due to seasonal CO_2 mass exchange [*Smith et al.*, 2001a; *Yoder et al.*, 2003; *Konopliv et al.*, 2006]. Range data to Viking, MGS, and ODY has permitted considerable improvement in knowledge of the orbit of Mars [cf. *Mayo et al.*, 1977; *Standish*, 2004; *Konopliv et al.*, 2006] over that estimated by purely astronomical methods. Errors in Mars ephemerides prior to the incorporation of MGS or Odyssey ranging, such as DE405 are $\sim$100 m [*Standish et al.*, 1992]. The uncertainties of the more recent DE411 and DE414 are 1 to 2 m in the Earth-Mars direction and $\sim$100 m in other directions [*Standish*, 2006]. Errors include contributions from the range tracking data (for Mars and other planetary spacecraft) discussed in section 2.3, in positions and masses of planets and asteroids [e.g., *Standish et al.*, 1992; *Standish and Newhall*, 1996], and relativistic effects [*Moyer*, 1971, 1981]. MRO data will be used to estimate range calibration biases for each DSN station location.

4.5.3. Phobos and Deimos

[50] The acceleration on the MGS and ODY spacecraft due to the gravitational attraction of the satellites of Mars is greater than 10% of the solar pressure force, and also exceeds the magnitude of the signals due to the solar tide and atmospheric drag [*Yuan et al.*, 2001; *Lemoine et al.*, 2001; *Konopliv et al.*, 2006]. The masses and orbits of Phobos and Deimos will be estimated in the global solution for the gravity field along with the mass of Mars.

5. Data Calibration and Processing

[51] The RS Gravity Team, in cooperation with the MRO Navigation Team, will monitor the performance of the MRO telecom system by routinely analyzing the tracking data for Doppler noise level, range biases and media affects. Monitoring of the data will occur separately at GSFC and JPL to allow independent quality checks, but due to proximity JPL team member Konopliv will provide quick looks. The Team will interact on a regular basis to assure that the quality of the tracking data is at the expected level.

6. Data Archiving and Distribution

[52] The RS Gravity Team will deliver Standard Data Products on the schedule specified by the Mars Reconnaissance Orbiter Archive Generation Validation and Transfer Plan. All geophysical parameters and data will be archived with the Geophysics Node of the Planetary Data System (PDS) at the Washington University, St Louis. Level 0 data (raw tracking observations) will be archived by the MRO Project. Level 1 and 2 data products will be delivered to the PDS for verification and archiving within 6 months of collection and will be disseminated to the scientific community immediately upon validation.

[53] Standard data products will include; spherical harmonic models of the static gravity field and areoid; error covariance models; maps of free air and Bouguer gravity and the aeroid; angular momentum desaturation events, and weather data.

[54] Additional data products that will be made available on a best efforts basis include: digital grids of free air and Bouguer gravity and the aeroid; digital grid of crustal thickness (incorporating MOLA topography [*Smith et al.*, 2001b]); seasonal changes in low degree gravity coefficients, updates in Mars dynamical parameters, Mars ephemeris, and precision orbits of the MRO spacecraft.

[55] Finally, WWW dissemination will be utilized for the rapid release of results of broad scientific or popular interest.

7. Summary

[56] The polar, low-periapsis orbit of the Mars Reconnaissance Orbiter and the high quality of its tracking system will collectively enable considerable improvement in the various radio science applications of the mission. Improvement is expected in the spatial resolution and of the global static field relevant to studies of the Martian interior. Extending the time series of the changes in the low-degree field beyond that provided by Mars Global Surveyor and Mars Odyssey will provide a decade-long quantitative record of the planet's seasonal cycle of CO_2 exchange. The data will also permit temporal sampling of the density of the Martian atmosphere relevant to the planet's general circulation and navigation of spacecraft. Finally, improvements in the knowledge of Martian dynamical parameters, the planet's ephemeris, and the masses of Phobos and Deimos are also expected.

[57] **Acknowledgments.** The Mars Reconnaissance Orbiter Radio Science Gravity Investigation is supported by the NASA Mars Exploration Program.

References

Albee, A. A., R. E. Arvidson, F. D. Palluconi, and T. Thorpe (2001), Overview of the Mars Global Surveyor mapping mission, *J. Geophys. Res.*, *106*, 23,291–23,316.

Asmar, S. W., J. W. Armstrong, L. Iess, and P. Tortora (2005), Spacecraft Doppler tracking: Noise budget and accuracy achievable in precision radio science observations, *Radio Sci.*, *40*, RS2001, doi:10.1029/2004RS003101.

Balmino, G., B. Moynot, and N. Valés (1982), Gravity field of Mars in spherical harmonics up to degree and order eighteen, *J. Geophys. Res.*, *87*, 9375–9746.

Barriot, J.-P., V. Dehant, W. Folkner, J.-C. Cerisier, A. Ribes, and J. Benoist (2001), The Netlander Ionosphere and Geodesy Experiment, *Adv. Space Res.*, *28*, 1237–1249.

Belleguic, V., P. Lognonné, and M. Wieczorek (2005), Constraints on the Martian lithosphere from gravity and topography data, *J. Geophys. Res.*, *110*, E11005, doi:10.1029/2005JE002437.

Bills, B. G. (1990), Venus topography: A harmonic analysis, *J. Geophys. Res.*, *95*, 14,131–14,136.

Chao, B. F., and R. S. Gross (1987), Changes in the Earth's rotation and low-degree gravitational field induced by large earthquakes, *Geophys. J. R. Astron. Soc.*, *91*, 569–596.

Chao, B. F., and D. P. Rubincam (1990), Variations of Mars' gravitational field and rotation due to seasonal CO_2 exchange, *J. Geophys. Res.*, *95*, 14,755–14,760.

Defraigne, P., O. de Viron, V. Dehant, T. V. Hoolst, and F. Hourdin (2000), Mars rotation variations induced by atmosphere and ice caps, *J. Geophys. Res.*, *105*, 24,563–24,570.

Dehant, V., P. Lognonne, and C. Sotin (2004), Network science, NetLander: A European mission to study the planet Mars, *Planet. Space Sci.*, *52*, 977–985.

Dombard, A. J., M. L. Searls, and R. J. Phillips (2004), An alternative explanation for the "Buried Channels" on Mars: The gravity signal from a sharp boundary on partially compensated, long-wavelength topography, *Geophys. Res. Lett.*, *31*, L05701, doi:10.1029/2003GL019162.

Folkner, W. M., R. D. Kahn, R. A. Preston, C. F. Yoder, C. D. Edwards, R. Hellings, E. M. Standish, M. Eubanks, and B. Bills (1997a), Mars dynamics from Earth-based tracking of the Mars Pathfinder lander, *J. Geophys. Res.*, *102*, 4057–4064.

Folkner, W. M., C. F. Yoder, D. N. Yuan, E. M. Standish, and R. A. Preston (1997b), Interior structure and seasonal mass redistribution of Mars from radio tracking of Mars Pathfinder, *Science*, *178*, 1749–1751.

Forbes, J. M., S. Bruinsma, and F. G. Lemoine (2006), Solar rotation effects on the thermospheres of Mars and Earth, *Science*, *312*, 1366–1368.

Gross, R. S., and B. F. Chao (1985), Excitation study of the LAGEOS-derived Chandler wobble, *J. Geophys. Res.*, *90*, 9369–9380.

Heiskanen, W. A., and H. Moritz (1967), *Physical Geodesy*, W. H. Freeman, New York.

Hess, S. L., R. M. Henry, and J. E. Tillman (1979), The seasonal variation of atmospheric pressure on Mars as affected by the south polar cap, *J. Geophys. Res.*, *84*, 2923–2927.

Hess, S. L., J. A. Ryan, J. E. Tillman, R. M. Henry, and C. B. Leovy (1980), The annual cycle of pressure on Mars measured by Viking landers 1 and 2, *Geophys. Res. Lett.*, *7*, 197–200.

Hilton, J. L. (1999), U.S. Naval Observatory ephemerides of the largest asteroids, *Astron J.*, *117*, 1077–1086.

Hoogenboom, T., and S. E. Smrekar (2006), Elastic thickness estimates for the northern lowlands of Mars, *Earth Planet. Sci. Lett.*, *248*, 830–839.

James, P. B., H. H. Kieffer, and D. A. Paige (1992), The seasonal cycle of carbon dioxide on Mars, in *Mars*, edited by H. H. Kieffer et al., pp. 934–968, Univ. of Ariz. Press, Tucson.

Karatekin, Ö., J. Duron, P. Rosenblatt, T. Van Hoolst, V. Dehant, and J.-P. Barriot (2005), Mars' time-variable gravity and its determination: Simulated geodesy experiments, *J. Geophys. Res.*, *110*, E06001, doi:10.1029/2004JE002378.

Kaula, W. M. (1966), *Theory of Satellite Geodesy*, Blaidsell, Waltham, Mass.

Kaula, W. M. (1979), The moment of inertia of Mars, *Geophys. Res. Lett.*, *6*, 194–196.

Keating, G. M., J. R. Murphy, R. F. Beebe, and L. F. Huber (2004), ODY-M-ACCEL-5-ALTITUDE-V1.0, NASA Planet. Data Syst., NASA Goddard Space Flight Cent., Greenbelt, Md. (Available at http://pds-atmospheres.nmsu.edu/data_and_services/atmospheres_data/odyacc.html)

Kiefer, W. S. (2004), Evidence for an extinct magma chamber beneath Syrtis Major, Mars: A look at the magmatic plumbing system, *Earth. Planet. Sci. Lett.*, *222*, 349–361.

Kieffer, H. H., B. M. Jakosky, and C. W. Snyder (1992), The planet Mars: From antiquity to present, in *Mars*, edited by H. H. Kieffer, et al., pp. 1–33, Univ. of Ariz. Press, Tucson.

King-Hele, D. (1987), *Satellite Orbits in an Atmosphere: Theory and Applications*, 291 pp., Blackie, London.

Konopliv, A., C. Yoder, E. Standish, D.-N. Yuan, and W. Sjogren (2006), A global solution for the Mars static and seasonal gravity, Mars orientation, Phobos and Deimos masses, and Mars ephemerides, *Icarus*, *182*, 23–50.

Lee, D. (2002), Measurement error for two-way coherent Doppler for MRO, interoffice memorandum, 15 pp., Jet Propul. Lab., Pasadena, Calif.

Lemoine, F. G., D. D. Rowlands, D. E. Smith, D. S. Chinn, D. E. Pavlis, S. B. Luthcke, G. A. Neumann, and M. T. Zuber (2001), An improved solution of the gravity field of Mars (GMM-2B) from Mars Global Surveyor, *J. Geophys. Res.*, *106*, 23,359–23,376.

Lemoine, F. G., S. Bruinsma, D. S. Chinn, and J. M. Forbes (2006), Thermospheric studies with Mars Global Surveyor, paper presented at AIAA/AAS Astrodynamics Specialist Conference, Am. Inst. of Aeronaut. and Astronaut., Keystone, Colo.

Leovy, C. B. (1985), The general circulation of Mars: Models and observations, *Adv. Geophys.*, *28a*, 327–346.

Lognonne, P., and B. Mosser (1993), Planetary seismology, *Surv. Geophys.*, *14*, 239–302.

Lognonne, P., et al. (1999), The NetLander Very Broadband seismometer, *Planet. Space Sci.*, *48*, 1289–1302.

Lowry, A. R., and S. Zhong (2003), Surface versus internal loading of the Tharsis rise, Mars, *J. Geophys. Res.*, *108*(E9), 5099, doi:10.1029/2003JE002111.

Magalhaes, J. A., J. T. Schofield, and A. Seiff (1999), Results of the Mars Pathfinder atmospheric structure investigation, *J. Geophys. Res.*, *104*, 8943–8955.

Mayo, A. P., W. T. Blackshear, R. H. Tolson, W. H. Michael Jr., G. M. Kelly, J. P. Brenkle, and T. A. Komarek (1977), Lander locations, Mars physical ephemeris, and solar system parameters: Determination from Viking lander tracking data, *J. Geophys. Res.*, *82*, 4297–4303.

Mazarico, E. M., M. T. Zuber, F. G. Lemoine, and D. E. Smith (2006), Atmospheric density during aerobraking of Mars Odyssey from radio tracking data, paper presented at AIAA/AAS Astrodynamics Specialist Conference, Am. Inst. of Aeronaut. and Astronaut., Keystone, Colo.

Mazarico, E., M. T. Zuber, F. G. Lemoine, and D. E. Smith (2007), Martian exospheric density using Mars Odyssey radio tracking data, *J. Geophys. Res.*, doi:10.1029/2006JE002734, in press.

McGovern, P. J., S. C. Solomon, D. E. Smith, M. T. Zuber, M. Simons, M. A. Wieczorek, R. J. Phillips, G. A. Neumann, O. Aharonson, and J. W. Head (2002), Localized gravity/topography admittance and correlation spectra on Mars: Implications for regional and global evolution, *J. Geophys. Res.*, *107*(E12), 5136, doi:10.1029/2002JE001854. (Correction, J. Geophys. Res., 109, E07007, doi:10.1029/2004JE002286, 2004.)

McKenzie, D., D. N. Barnett, and D. N. Yuan (2002), The relationship between Martian gravity and topography, *Earth Planet. Sci. Lett.*, *195*, 1–16.

Miller, J. K. (1993), The effect of clock, media and station location errors on Doppler measurement accuracy, *Telecommun. Data Acquisition Prog. Rep., 42-113*, Jet Propul. Lab., Pasadena, Calif.

Moyer, T. D. (1971), Mathematical formulation of the double-precision orbit determination program (DPODP), *JPL Tech. Rep. 32-1527*, Jet Propul. Lab., Pasadena, Calif.

Moyer, T. D. (1981), Transformation from proper time on Earth to coordinate time in solar system barycentric space-time frame of reference, part I and part II, *Celestial Mech.*, *23*, 33–68.

Neumann, G. A., D. D. Rowlands, F. G. Lemoine, D. E. Smith, and M. T. Zuber (2001), Crossover analysis of Mars Orbiter Laser Altimeter data, *J. Geophys. Res.*, *106*, 23,753–23,768.

Nier, A. O., and M. B. McElroy (1977), Composition and structure of Mars' upper atmosphere: Results from the neutral mass spectrometers on Viking 1 and 2, *J. Geophys. Res.*, *82*, 4341–4349.

Pavlis, D. E., S. G. Poulouse, S. C. Rowton, and J. J. McCarthy (2001), *GEODYN Operations Manuals*, contractor report, Raytheon ITTS, Lanham, Md.

Pavlis, D. E., S. Poulose, and J. J. McCarthy (2006), GEODYN operations manuals, contractor report, SGT Inc., Greenbelt, Md.

Phillips, R. J., et al. (2001), Ancient geodynamics and global-scale hydrology on Mars, *Science*, *291*, 2587–2591.

Rowlands, D. D., D. E. Pavlis, F. G. Lemoine, G. A. Neumann, and S. B. Lutchke (1999), The use of crossover constraint equations derived from laser altimetry in the orbit determination of Mars Global Surveyor, *Geophys. Res. Lett.*, *26*, 1191–1194.

Rubincam, D. P. (1984), Postglacial rebound observed by LAGEOS and the effective viscosity of the upper mantle, *J. Geophys. Res.*, *89*, 1077–1087.

Sanchez, B. V., D. D. Rowlands, R. M. Haberle, and J. Schaeffer (2003), Atmospheric rotational effects on Mars based on the NASA Ames general circulation model, *J. Geophys. Res.*, *108*(E5), 5040, doi:10.1029/2002JE001984.

Saunders, R. S., et al. (2004), Mars Odyssey mission summary, *Space Sci. Rev.*, *110*, 1–36.

Schofield, J. T., J. R. Barnes, D. Crisp, R. M. Haberle, S. Larsen, J. Mangalhaes, J. R. Murphy, A. Seiff, and G. Wilson (1997), The Mars Pathfinder atmo-

sphere structure investigation: Meteorology (ASI/MET) experiment, *Science*, *278*, 373–375.
Searls, M. L., W. B. Banerdt, and R. J. Phillips (2006), Utopia and Hellas basins, Mars: Twins separated at birth, *J. Geophys. Res.*, *111*, E08005, doi:10.1029/2005JE002666.
Seiff, A., and D. B. Kirk (1977), Structure of the atmosphere of Mars in summer mid-latitudes, *J. Geophys. Res.*, *82*, 4364–4378.
Shambayati, S., D. Morabito, J. S. Border, F. Davarian, D. Lee, R. Mendoza, M. Britcliffe, and S. Weinreb (2006), Mars Reconnaissance Orbiter Ka-band (32 GHz) demonstration: Cruise phase operations, paper presented at Spaceops 2006 Conference, Am. Inst. of Aeronaut. and Astronaut., Rome.
Short, O. G., J. F. McKinney, C. W. McAnally, J. Beerer, and P. Theisinger (1996), Mars Global Surveyor Telemetry Calibration Handbook, *MCR-95-4158*, 363 pp., Jet Propul. Lab., Pasadena, Calif.
Smith, D. E., F. J. Lerch, R. S. Nerem, M. T. Zuber, G. B. Patel, S. K. Fricke, and F. G. Lemoine (1993), An improved gravity model for Mars: Goddard Mars Model-1 (GMM-1), *J. Geophys. Res.*, *98*, 20,781–20,889.
Smith, D. E., W. L. Sjogren, G. L. Tyler, G. Balmino, F. G. Lemoine, and A. S. Konopliv (1999a), The gravity field of Mars: Results from Mars Global Surveyor, *Science*, *286*, 94–96.
Smith, D. E., M. T. Zuber, R. M. Haberle, D. D. Rowlands, and J. R. Murphy (1999b), The Mars seasonal CO_2 cycle and the time variation of the gravity field: A general circulation model simulation, *J. Geophys. Res.*, *104*, 1885–1896.
Smith, D. E., et al. (1999c), The global topography of Mars and implications for surface evolution, *Science*, *284*, 1495–1503.
Smith, D. E., M. T. Zuber, and G. A. Neumann (2001a), Seasonal variation of snow depth on Mars, *Science*, *294*, 2141–2146.
Smith, D. E., et al. (2001b), Mars Orbiter Laser Altimeter: Experiment summary after the first year of global mapping of Mars, *J. Geophys. Res.*, *106*, 23,689–23,722.
Smrekar, S. E., G. E. McGill, C. A. Raymond, and A. M. Dimitriou (2004), Geologic evolution of the Martian dichotomy in the Ismenius area of Mars and implications for plains magnetization, *J. Geophys. Res.*, *109*, E11002, doi:10.1029/2004JE002260.
Sniffin, R., S. Slobin, D. Morabito, A. Bedrossian, D. Shin, and L. Paul (2000), *DSMS Telecommunications Link Design Handbook*, *CL 06-2686, Rev. E*, Jet Propul. Lab., Pasadena, Calif.
Sohl, F., and T. Spohn (1997), The interior structure of Mars: Implications from SNC meteorites, *J. Geophys. Res.*, *102*, 1613–1635.
Srinivasan, D. K., M. E. Perry, K. B. Fielhauer, D. E. Smith, and M. T. Zuber (2007), Application of the MESSENGER radio frequency subsystem to meet the mission radio science objectives, *Space Sci. Rev.*, in press.
Standish, E. M. (2004), The astronomical unit now, in *Proceedings of the IAU Colloquium 196, Transits of Venus: New Views of the Solar System and Galaxy*, Univ. of Central Lancashire, Preston, Lancashire, UK.
Standish, E. M. (2006), JPL Planetary Ephemeris DE414, *JPL IOM 343R-06-002*, Jet Propul. Lab., Pasadena, Calif., 21 April.
Standish, E. M., and X. X. Newhall (1996), New accuracy levels for solar system ephemerides, in *Dynamics, Ephemerides and Astronomy of the Solar System*, *IAU Symp.*, vol. 172, edited by S. Ferraz-Mello, B. Morando, and J. Arlot, pp. 29–36, Int. Astron. Union, Paris.
Standish, E. M., X. X. Newhall, J. G. Williams, and D. K. Yeomans (1992), Orbital ephemerides of the Sun, Moon, and planets, in *Explanatory Supplement to Astronomical Almanac*, edited by P. K. Seidelmann, pp. 279–323, Univ. Sci., Mill Valley, Calif.
Tolson, R. H., G. M. Keating, S. N. Noll, D. T. Baird, and T. J. Shellenberg (1999), Utilization of Mars Global Surveyor accelerometer data for atmospheric modeling, in *Astrodynamics 1999: Proceedings of the AAS/AIAA Astrodynics Conference*, edited by K. C. Howell, pp. 99–386, Univelt, San Diego, Calif.
Tracadas, P. W., M. T. Zuber, D. E. Smitha, and F. G. Lemoine (2001), Density structure of the upper thermosphere of Mars from measurements of air drag on the Mars Global Surveyor spacecraft, *J. Geophys. Res.*, *106*, 23,349–23,357.
Turcotte, D. L., and G. Schubert (1981), *Geodynamics: Applications of Continuum Physics to Geologic Problems*, p. 450, John Wiley, Hoboken, N. J.
Turcotte, D. L., R. Shcherbakov, B. D. Malamud, and A. B. Kucinskas (2002), Is the Martian crust also the Martian elastic lithosphere?, *J. Geophys. Res.*, *107*(E11), 5091, doi:10.1029/2001JE001594.
Tyler, G. L., et al. (1992), Radio science investigations with Mars Observer, *J. Geophys. Res.*, *97*, 7759–7779.
Tyler, G. L., G. Balmino, D. P. Hinson, W. L. Sjogren, D. E. Smith, R. A. Simpson, S. W. Asmar, P. Priest, and J. D. Twicken (2001), Radio science observations with Mars Global Surveyor: Orbit insertion through one year in mapping orbit, *J. Geophys. Res.*, *106*, 23,327–23,348.
VanDecar, J., et al. (2001), Mars Insight Issue, *Nature*, *412*, 207–253.
Van den Acker, E., T. Van Hoolst, O. de Viron, P. Defraigne, F. Forget, F. Hourdin, and V. Dehant (2002), Influence of the seasonal winds and the CO_2 mass exchange between atmosphere and polar caps on Mars' rotation, *J. Geophys. Res.*, *107*(E7), 5055, doi:10.1029/2000JE001539.
Van Hoolst, T., V. Dehant, and P. Defraigne (2000), Chandler wobble and free core nutation for Mars, *Planet. Space Sci.*, *48*, 1145–1151.
Wieczorek, M. A., and R. J. Phillips (1998), Potential anomalies on a sphere: Applications to the thickness of the lunar crust, *J. Geophys. Res.*, *103*, 1715–1724.
Wieczorek, M. A., and M. T. Zuber (2004), Thickness of the Martian crust: Improved constraints from geoid-to-topography ratios, *J. Geophys. Res.*, *109*, E01009, doi:10.1029/2003JE002153.
Withers, P. (2006), Mars Global Surveyor and Mars Odyssey Accelerometer observations of the Martian upper atmosphere during aerobraking, *Geophys. Res. Lett.*, *33*, L02201, doi:10.1029/2005GL024447.
Yoder, C. F., A. Konopliv, D.-N. Yuan, E. Standish, and W. Folkner (2003), Fluid core size of Mars from detection of the solar tide, *Science*, *300*, 299–303.
You, T.-H., M. D. Johnston, E. Maize, and J. E. Graf (2005), Mars Reconnaissance Orbiter Navigation Plan, *JPL D-22240, MRO 31-202, Rev. B*, 124 pp., Jet Propul. Lab., Pasadena, Calif.
Yuan, D. N., W. L. Sjogren, A. S. Konopliv, and A. B. Kucinskas (2001), The gravity field of Mars: A 75th degree and order model, *J. Geophys. Res.*, *106*, 23,377–23,401.
Zuber, M. T. (2001), The crust and mantle of Mars, *Nature*, *412*, 220–227.
Zuber, M. T., and D. E. Smith (2006), Variations in the masses of the seasonal polar icecaps over three Mars years, paper presented at Fourth International Conference on Mars Polar Science and Exploration, Lunar and Planet. Inst., Davos, Switzerland.
Zuber, M. T., et al. (2000), Internal structure and early thermal evolution of Mars from Mars Global Surveyor topography and gravity, *Science*, *287*, 1788–1793.
Zurek, R. W., and S. E. Smrekar (2007), An overview of the Mars Reconnaissance Orbiter (MRO) science mission, *J. Geophys. Res.*, *112*, E05S01, doi:10.1029/2006JE002701.
Zurek, R. W., J. R. Barnes, R. M. Haberle, J. B. Pollack, J. E. Tillman, and C. B. Leovy (1992), Dynamics of the atmosphere of Mars, in *Mars*, edited by H. H. Kieffer et al., pp. 835–933, Univ. of Ariz. Press, Tucson.

S. W. Asmar, A. S. Konopliv, and S. E. Smrekar, Jet Propulsion Laboratory, 4800 Oak Grove Drive, Pasadena, CA 91109, USA. (sami.w.asmar@jpl.nasa.gov; alex.konopliv@jpl.nasa.gov; ssmrekar@jpl.nasa.gov)

F. G. Lemoine and D. E. Smith, Solar System Exploration Division, NASA Goddard Space Flight Center, Greenbelt, MD 20771, USA. (frank.lemoine@gsfc.nasa.gov; david.e.smith@nasa.gov)

M. T. Zuber, Department of Earth, Atmospheric, and Planetary Sciences, Massachusetts Institute of Technology, 54-518, 77 Massachusetts Avenue, Cambridge, MA 02139-4307, USA. (zuber@mit.edu)